How to prevent endothelial cells from losing their edge: a simple patterning of development-like matrix guides a microvessel morphogenetic process by self-organization

Ana Ximena Monroy-Romero[1,2] , Brenda Nieto-Rivera[2] , Wenjin Xiao[2] , Mathieu Hautefeuille[2,*]

[1] Programa de Doctorado en Ciencias Biomédicas, Universidad Nacional Autónoma de México, México

[2] Laboratoire de Biologie du Développement (UMR 7622), Institut de Biologie Paris Seine, Sorbonne Université, 75005 Paris, France

*Corresponding author: Mathieu Hautefeuille.

Email: mathieu.hautefeuille@sorbonne-universite.fr

Competing Interest Statement: The authors declare no competing interest

Author Contributions: A.X.M.-R and M.H. designed research; A.X.M.-R, B.N.-R, W.X. and M.H performed research; A.X.M.-R analyzed data; A.X.M.-R and M.H. wrote the paper, A.X.M.-R, B.N.-R, W.X. and M.H reviewed and edited the paper.

Abstract

Vascular engineering seeks to generate reliable models for studying cellular interactions in the context of preserving homeostasis and disease development. However, current systems mainly focus on recapitulating large blood vessels embedded in thick extracellular matrix gels or do not address discontinuous capillaries, crucial microvascular structures. By adapting a Marangoni flow-driven protein densification process on GelTrex domes, we promoted the self-organization of endothelial cells into mature lumenized vessels by anisotropic directional organization following an edge micropattern. Our findings revealed a sequential morphogenetic process leading to microvessels with both murine and human immortalized liver sinusoidal endothelial cells (LSECs). Differential behaviors were found on the whole sample and cell migration, proliferation and polarization were guided by this pattern to form a long multicellular cord. Cells forming this structure deformed large regions of the dome, generating a wave-like fold all around it, hinged in a laminin depletion zone. This wrapped the cell cords with proteins from the gel which marked the beginning of a lumenogenesis process, regulated by a change in the apico-basal polarization of the cord cells, followed by maturation of tight junctions, remodeling of the extracellular matrix, and formation of a lumen; all steps reported in *in vivo* vessel development. Furthermore, we demonstrate that the geometry of the vessels can be controlled by initial topography of the gel. We believe our simple fabrication method, guiding an autonomous self-organization of vessels without the need for supporting cells or complex prefabricated scaffolds, is suitable for future integration into microphysiological systems of discontinuous, fenestrated capillaries.

Main Text

Introduction

Extensive efforts have been made to engineer accurate morphofunctional vessels of varying calibers *in vitro*, either to decipher endothelial functions, study mechanistic processes, or to enhance their overall restoration inside microphysiological systems (MPS). One strategy follows a top-down approach, where a voided tubular scaffold is pre-fabricated inside a collagen gel. Typically, a confluent monolayer of human umbilical vein endothelial cells (HUVEC) is established, lining the scaffold's inner wall which enables perfusion, exposure to controlled mechanical stimuli (1, 2), and co-culture environments (3, 4). Nevertheless, the dimensions of these models are restricted by their fabrication process and end up imitating only large vessels covered by a thick extracellular matrix (ECM), failing to recapitulate smaller capillaries. An alternative approach is a bottom-up engineering strategy that guides endothelial cells (ECs) to self-organize, following developmental processes such as vasculogenesis (*de novo* vessel formation) and angiogenesis (the sprouting of new vessels from pre-existing ones). For the latter, a porous ECM hydrogel generates growth factor gradients, which guide angiogenic sprouts from side channels hosting EC monolayers (5). The resulting spontaneous emergence of a capillary bed inside the EC-laden gels is widely employed to restore perfusable and permeable microvessels inside MPS. These architectures have been particularly successful in vascularizing several types of tissues, including those co-cultured on top of -or embedded within- the gel, like tumor microenvironments (6). These models are gaining an increasing importance in MPS technology, but fail to present specific microenvironments where capillary microvessels possess a discontinuous or fenestrated basement membrane (BM). Such characteristics render their ECs susceptible to slight deformation to pressure, shear and changes in surrounding stiffness (7). Liver sinusoids are one such specialized capillaries, featuring highly porous microvessels with a discontinuous BM composed mainly of laminin and collagen IV, as well as microscopic *fenestrae (8)*. These unique attributes make liver sinusoidal endothelial cells (LSECs) highly permeable (9) but also extremely responsive to mechanics, and their response to changes in their surroundings can in turn significantly impact the entire microenvironment (10, 11). The mechanisms at play in liver sinusoidal capillarization (including the loss of *fenestrae*) under mechanical stress are not elucidated, primarily due to the absence of an appropriate model. Such a model would need a perfusable, standalone microvessel design with defined ECM and BM composition, stiffness and permeability, incorporating LSECs in co-culture with hepatocytes and hepatic stellate cells. These requirements cannot be fulfilled by the current capillary bed models that are embedded and clamped within a fixed ECM gel.

The vasculogenesis assay provides a solution for constructing non-embedded microvessels (12) . The process is inspired by the natural process of vasculogenesis, which involves five steps: 1) endothelial specification from angioblasts, 2) recruitment of cells into multicellular cords, 3) lumenogenesis, 4) ECM remodeling, and 5) recruitment of supporting cells if necessary (13). In this assay, the recruitment of endothelial cells into a network of thin but stable multicellular cords (also referred as tubes) can be effectively recapitulated *in vitro*. It employs a reconstituted murine basement membrane coating (Matrigel™, GelTrex™ or a commercial alternative) as the culture substrate, imitating the ECM composition during early development. The underlying mechanisms behind this spontaneous, cell autonomous organization are predominantly mechanical. It was indeed demonstrated that the interplay between the mechanical plasticity of laminin and the contractility of cells allows neighboring cells to mechanically sense one another, polarize and migrate towards each other, while reorganizing and densifying the surrounding ECM they deform (14, 15). Upon appropriate conditions, with a suitably soft ECM and adequate cell density (meeting the initial cell-cell distance required to initiate the aforementioned process), paths of increased tension act as guiding cues for cell migration, resulting in cord-like networks sitting on top of the matrix (i.e., non-embedded microvessels). However, this structure lacks ordered or preferential organization necessary for future directional flow. The orientation of these cords is indeed random and they lack key characteristics to be considered morphofunctional vessels. Notably, the presence of a lumen in the network is not demonstrated and the internal perfusion remains unattained due to their insufficient maturity (as demonstrated in our work, as detailed below). Luminal flow plays a crucial role in development, preservation, function, and health of vessels in vivo. For instance, it defines the venule or arteriole identity (16), influences sprouting and vascular remodeling (17), and when perturbed, can lead to pathologies (10, 18). Therefore, it is vital to ensure that cell cords developed *in vitro* can mature into perfusable structures. To achieve this aim, shear stress is pivotal, as it is key in the gradual formation of a microvessel architecture. However, the random directions taken by ECs in such a cord formation likely leads to a short-ranged, multidirectional shear that proves insufficient for further vessel maturation and possible lumenogenesis.

Lumenogenesis is the process of lumen formation, transitioning 2D cords to 3D vessels, necessary for the passage of flow through vessels without disrupting endothelial cell-cell junctions and barrier function. This complex process requires the coordination of multiple cellular and molecular events. It is initiated by the establishment of an apicobasal polarization of the multicellular cord-like structure, characterized by the trafficking of apical membrane proteins such as Podocalyxin (PDCLX), to internal sites of cell-cell contact also known as the apical membrane initiation site (AMIS) (19, 20). Interestingly, laminin is known to provide directional cues for polarization (21–23). After polarization and onset of lumen formation, tight junctions undergo maturation, evidenced by zona occludens-1 protein (ZO-1) localization shifting from cytoplasmic condensates to junctional sites, influenced by increased pressure (24). Simultaneous to the full lumen appearance probably in response to internal pressure build-up, F-actin is recruited to the apical cell surface. Endothelial cells also generate the force required for lumen expansion and preservation, which requires flow to maintain a functional vessel (25). Finally, the BM is gradually modified by secretion and organized locally to meet the vessel's new mechanical support requirements (26). All these controls and validation cues are important to address when striving to achieve physiological relevance in engineered microvessels for *in vitro* MPS applications. It is thus critical to propose a new vascular model that recapitulates a BM-free liver sinusoid with the microvessel dimensions and not deeply embedded in a gel. This model holds significant promise as it could allow the study of how LSECs respond to mechanical stress induced by blood flow. This stress is hypothesized to initiate perturbations in the metabolic and hemodynamic features of liver sinusoids, potentially contributing to the development of liver diseases (27). However, current models are unable to provide the necessary level of recapitulation of native conditions, to carefully study these mechanisms and reach a definitive conclusion regarding the validation or refutation of this hypothesis. Therefore, developing non-embedded capillaries-on-chip systems becomes essential, as they could offer valuable insights into these complex biological phenomena.

In this work, we proposed to imitate developmental biology and guide cell self-organization to form a lumenized capillary that closely resembles the liver sinusoid. The rationale behind this approach was that a thin laminin pattern could provide the necessary positional cues to guide the transition from a 2D cord-like structure to a 3D polarized and lumenized microvessel. This transition occurs when cells align into cords and polarize, as

suggested in the work by Tracqui and colleagues (28). However, 2D cords formed in vasculogenesis assays are randomly organized structures and usually immature, lacking spatial signals to trigger lumenogenesis. The challenge was to coat the entire external (abluminal) side of all interconnected cells in the preformed cords with laminin to add such signals, but without embedding and clamping them in a thick ECM, absent from the liver sinusoid physiology. Thus, we developed a novel method for culturing LSECs on a GelTrex soft gel with a thin pattern of anisotropic laminin and collagen IV at the edge. This topographical guidance was obtained using a Marangoni flow-derived patterning, inspired by a previous work from Nerger *et al.* (29). By precisely controlling the evaporation rate during gelation of a soft ECM hydrogel sessile droplet ('dome' shape), a high protein density is localized at a thin peripheral edge. This micropattern successfully confined LSECs in a peripheral train, providing a longer sustained, unidirectional guidance of EC cord organization. Following an initial slow approach phase, EC preferentially aligned upon adhesion, capitalizing on the enhanced cell growth at the edge of adherent patterns (30). Mechanical deformation from the cord along the edge of the dome then triggered a piecewise folding of the soft gel wall, leading to a wave-like blanketing of cells. This process resulted in a complete coating of the cell cord with laminin, facilitating a gradual apico-basal cell polarization and the subsequent cues leading to lumenogenesis. The maturation of the tight junction was verified through the change of localization of ZO-1 protein, while mechanical support from the actin cytoskeleton was evidenced by the concentration of F-actin in the apical face of the structure. Ultimately, the entire process yielded a lumenized vascular structure around the dome. This newly established model was primarily focused on deciphering the morphogenetic process, with a future perspective of an application as a perfusable and non-embedded microvessel by achieving a straight vascular structure.

Results

Gelation of a sessile droplet of GelTrex densifies the deposition of Laminin and Collagen IV in a ring-like pattern at the edge

First, we sought to deposit an anisotropically oriented, high-density pattern of laminin and collagen IV to guide cell adhesion, proliferation and migration in one preferential direction. To do this, we employed an ECM material, GelTrex™ (GT), which is composed of 60% of laminin and 30% of collagen IV. The gelation / evaporation rate of a GT droplet deposited on a silanized glass coverslip was controlled by placing it inside a cell culture incubator for 30 min (Figure 1A). Three zones on the dome were identified by using scanning electron microscopy (SEM): middle, near edge and edge (Figure 1B) with clear differences in the ECM density between each other (Figure 1C). The ECM density, as determined by the network filling factor, demonstrated the highest value at the edge (98.13% ± 1.02%), and significantly lower in the central middle region (68.17% ± 5.58%) (Figure 1D). Moreover, the diameters of the identified pores were smaller at the edge (51.46 nm ± 8.33 nm) than those in the middle of the dome (357.80 nm ± 136.78 nm), indicating a gradient of ECM density in the gelated GT dome, with a highly dense edge. The mechanical results from nanoindentation aligned with the observed increase of ECM density, revealing a radial increase in the Young's modulus towards the periphery. Specifically, a value of 245.5 Pa ± 40.3 Pa was found at the center of the domes, consistent with results from other reconstituted BM gels (31). However, it drastically and locally increased to 439.5 Pa ± 156.2 Pa at the very edge. It is worth noting that this value may be subject to the influence of the glass substrate stiffness close to the edge, where the reduced thickness of the gel becomes non-negligible (32).

Next, we examined the distribution of laminin and collagen IV following the gelation of the dome by using immunostaining (Figure 1E). Both proteins exhibited a distinct high concentration in a ring-like pattern at the edge of the dome, a characteristic result of Marangoni flows. Their profiles were analyzed transversally and inwards through the dome (yellow arrow in figure 1E) and the full width at half maximum (FWHM) was measured for both signals. A thinner (16.78 µm ± 3.89 µm) laminin signal was revealed compared to that of collagen IV (44.75 µm ± 4.54 µm), as shown in Figure 1F, where the edge of the dome is defined as the origin. Importantly, the laminin region can be denominated as a pattern, given its order of magnitude relative to a single cell size. Previous studies have shown that such narrow patterns could guide EC spreading, orientation and migration (33). This finding is particularly relevant to our efforts in confining cell growth and migration on laminin to align multicellular cords along one single, anisotropic path. We have identified these optimal conditions through testing alternative experimental parameters, all of which ultimately proved ineffective (see supplementary text, Figure S1 and S2).

Liver sinusoidal endothelial cells form tubular structure following the edge of a GelTrex dome.

The Marangoni-flow dome construction method yielded a substrate with a pattern of densified laminin and collagen IV, in contrast to the uniform, flat ECM layer observed in traditional vasculogenesis assays. Given this difference in substrate organization, we posited that our dome could guide LSECs to self-organize in a preferred direction, as opposed to the random cord pattern.

Immortalized liver sinusoidal endothelial cells (TSECs) (34) were cultured on GT domes and their organization was followed over time (Figure 2A). Three distinct types of structure emerged based on cell localization in the sample: (1) TSECs formed a monolayer on the glass surrounding the dome; (2) In the middle of the dome, within 24 hours cells rapidly organized into a cord network resembling the structures formed in traditional self-organization assays performed on Matrigel or GelTrex; (3) Interestingly, a few cells that had adhered on glass close to the dome's edge gradually attached to it (zoomed region of Figure 2A) and formed a thin but discernible structure all around it. After 48 hours of culture, the cells in the middle of the dome were completely organized into a randomly oriented network of relatively short branches. Simultaneously, a long, thin, single cord had already formed following the whole periphery of the dome at its edge. The structure at the edge also connected with the network formed at the middle of the dome at a few contact points. Furthermore, at 96 hours a new feature was observed, a front moving away gradually from the original dome edge (indicated with a yellow arrow in Figure 2A and quantified in 2B); it was later demonstrated to be a small portion of the GelTrex dome displaced by the cells (Figure 7B). Immunostaining for VE-cadherin revealed a lumenized structure (Figure 2C).

SEM inspection of samples cultured for 96 hours helped characterize the different multicellular architectures. It revealed distinct cellular morphological shapes adopted by the TSECs in these three different regions. The monolayer on the glass (Figure 3A) was composed of cells with a cobblestone morphology, a characteristic of monolayers. These cells presented a high density of microvilli, structures associated with pathological LSECs (35). The cords at the center of the domes appeared to be in the process of forming tubes. These multicellular structures were composed of slightly curved cells that had no microvilli (Figure 3B). They exhibited zipped cell-cell junctions, but in certain regions, these junctions appeared loose and not mature for a vessel, with clear openings between neighboring cells. Submicron pores, indicative of LSEC *fenestrae*, were also observed in these structures (zoomed in Figure 3B). Additionally, the cords appeared only simply sitting on top of the ECM, lacking apparent interaction with the underlying ECM, contrary to what was described by (15) where ECs organized the surrounding matrix to stabilize the cords. In contrast, the cells forming the peripheral structure were organized into more stable microvessels with elongated, thinner structures resembling tubes over the whole dome edge. Compared with the central cords, these tubes appeared to be covered by a thin ECM coating, and no cell membrane or cell-cell junction structures were visible beneath it. Over time, this coating thickened and aligned into a BM, depicting vessel maturation (Figure 8E). Complete evolution of this structure is presented in supplementary Figure 3. Compared to the central network, this type of cord showed many more adherent interactions with the lining ECM from the dome edge, and no apparent contact with the neighboring outer monolayer, consistent with our observations of monolayer detachment without perturbing the tube in later times. Importantly, this differential organization was also observed with TMNK-1 cells, a human immortalized LSEC cell line (36), showing it is not a cell line specific feature (Supplementary Figure 4). These results show that the engineered sessile droplet of GT, in a soft dome-shape substrate, instructs LSECs to self-organize differently depending on ECM density and organization. Thanks to LSEC high contractility (37), cord networks also formed in areas with randomly organized ECM at the center of the dome, similar to conventional vasculogenesis assays. Regions along the edge exhibited a more stable, vessel-like morphology with a preferential orientation.

Progressive morphogenetic steps at the edge of the GelTrex dome enable a lumenized microvessel formation

Further investigations were conducted to elucidate the precise morphogenetic steps followed by edge cells in constructing this aligned tube. We imaged the cells for five days through phase contrast live-imaging to understand the dynamic behavior of TSECs, particular attention was placed on the edge of the dome, leaving the central part of the dome out of the study. Four stages were identified as crucial to guarantee the generation of a

tubular structure with a preferred tangential direction. We studied each of these steps individually to precisely describe the morphogenetic process leading to a tube formation around the dome substrate.

Stage 1: formation of a long, 1-cell thin train along the dome edge. Since the earliest moments of culture, cell dynamics followed a preferential migration/proliferation pattern. Once adhered to glass, in the first 24 hours, only cells in close proximity to the edge of the dome began migrating towards it (Figure 4A, Movie S1). The initial cells and their daughters after mitosis were tracked during the first day of culture and the evolution of the straight distance between their closest border and the dome was measured. Figure 4B shows a clear threshold of 50 µm, equivalent to 4 cell sizes, below which cultured TSECs unequivocally migrated toward the dome, while cells further away stayed apart or moved away. The preferred attraction directionality during this approach phase was evaluated by measuring the angle between the tangent to the dome edge and the direction of cell migration. Before attachment, no specific angle was found, resulting in a broad distribution of approaching angles per cell and per hour, ranging from 6° and 162° (Figure 4C). However, after attachment to the dome's edge, the direction of migration remained anisotropic, with cells permanently residing at the edge, depicted with an angle of either 180° or 0° depending on the clockwise or anticlockwise direction of the migration following contact (Figure 4D). We noted that during migration, cell persistence was also maintained by a preferred direction of division, following the mother cell's previous guidance. This occurred in both approach and adherent phases, as depicted in the representative examples of Figure 4A with white (approach) and yellow (adherent) arrows. Importantly, the morphogenetic structures that self-organized on the gel remained disconnected from the monolayer (Figure 7C), which sometimes detached when confluent without disrupting the cords and tubes. This behavior did not occur only when the initial cell density was too high. In such cases, a monolayer migration front reached the dome edge before the onset of stage 1, effectively covering the gel after 1-2 days and impeding this step (Supplementary Figure 1E).

Stage 2: formation of a multicellular cord around the dome. When adhered to the dome's edge, cells continued migrating and proliferating exclusively in the tangential direction, gradually covering the entire edge (Figure 5A, Movie S2). Two or three days after seeding, a gradual change in the organization resulted in two distinct structures at the same location but at different heights. To examine cell movement and dome deformation during these processes, we stained the cells with phalloidin and performed an immunofluorescence against laminin 111, the principal component of GelTrex. Through confocal microscopy, stage 2 and stage 3 were identified (Figure 5B). Transversal views of the samples in stage 2, showed that the cell architecture transitioned from a stable 1-cell train structure (1D) at the edge towards a thicker, 2D multicellular cord that followed the same orientation around the entire dome. This cord consisted of 3 cells in thickness , with cells being more spreaded out at the bottom of the gel and more elongated above (Figure 5A, white arrow). This thickening was associated with a change in the direction of proliferation and resulted in a new train of cells forming further up the edge. This process was observed all along the dome edge (Figure 5A, bottom line) and eventually led to localized and piecewise ECM displacements, which are characteristic of stage 3.

Stage 3: formation of an ECM folding pattern. Immediately after the transition of a 1D-train to a 2D cord architecture, the most critical morphogenetic step occurred, going from 2D to 3D. This step started with an outwards displacement of the gel edge, and immunofluorescence imaging showed that it resulted from the folding of the gel, which was driven by a local indentation of the gel substrate on the dome, consistently occurring beneath a central "hinge cell" (Figure 5B, stage 3). This indentation was quantified by measuring the progression of folding angle (Figure 5C). The angle gradually decreased from a flat substrate (180° at stage 2) to an impressive 60° folding after 24 hours. Importantly, this angle contributed to both cell and dome folding, similarly to an ocean surf wave progressing outwards to the shore. Following this analogy, at smaller angles the plunging break rapidly converted into a collapse break, making it challenging to measure the progression of folding accurately (Figure 7D).

Processes of folding have been mainly attributed to the constriction of an apically localized actomyosin network. However, in our observations, there was no indication of such an active process driving the folding. Instead, a local reduction of the ECM density was consistently shown at the basal side of the hinge cell, precisely where the angles were measured (Figure 5D-E). A decrease in the laminin signal below the hinge cell (when

compared to its neighboring cells) was confirmed, compared to that the one of its neighboring cells, with a more significant contrast as the folding progressed (starting with a 25% difference in stage 2 and up to 36% at the latest observable instant of stage 3). This observation is in line with a previous report where a localized ECM depletion at the basal side of certain epithelial cells was responsible for the developmental morphogenetic process underlying the formation of the Drosophila wing (38).

As previously mentioned, the folding process occurred around the entire dome. It was independent of the dome size for all domes tested in the 5 - 80μL range (not shown). However, it happened in a piecewise fashion, with all the pieces progressing and connecting to each other after a few hours. In order to elucidate the dynamics behind the folding, live-imaging analysis of this 2D to 3D process was performed on a GelTrex dome incorporated with fluorescent beads (Figure 6). This allowed us to track the displacement of the beads every 30 minutes, starting after the cord had formed at the edge of the dome and until the start of the folding. Figure 6A shows a typical temporal evolution of the displacement of the beads and its analysis suggests that the observed folding is a passive response following a lateral pulling on the outside. Two distinct regions of interest stood out during the experiments, as depicted by the groups of displacement vectors. First, localized lateral displacements appeared in locations where the cord had thickened due to non-tangential local proliferation of cells (purple boxes). These regions appeared almost periodically (every 300 to 500 μm, delimited by white dashed lines) and were responsible for the piecewise nature of this process. Between them,a third, central region (green box) was defined, where bead displacements always occurred posterior to the lateral ones, with no apparent proliferation. The lateral strains that appeared first showed a lateral and tangential direction, almost symmetrical with respect to the center region. The bead displacement of the central region occurred 2 hours after the lateral stretch, with an inwards direction, resembling a retraction, and had a larger amplitude. The central inwards folding event (Figure 6B) led to an ECM blanket covering the cells and curling back inside (Figure 6D), which explains the bead displacement at the central region. The overall process is summarized in the global displacement persistence image constructed in Figure 6E. Stage 3 is thus characterized as a cell-provoked, tension-driven folding where the laminin-rich ECM slowly blanket-rolls the dome edge where cells are aligned as a multicellular cord, first by covering it and then curling back inwards (Supplementary figure 5).

Stage 4: ECM enclosure of the multicellular cord and vessel maturation. The final morphogenetic step corresponds to the completion of the ECM folding surrounding the cell cord as a blanket-roll shape (Figure 7 and Supplementary Figure 5). This event is simultaneous with the continued ECM displacement away from the dome edge and sliding out, similar to a wave landing on the shore (Figure 7A). This displacement can be correlated with the structure moving from the edge as quantified in figure 2B. A vessel-like structure was established at the edge around the entire dome. It features a capillary-sized architecture with only 3 or 4 cells facing each other, within an ECM roll. The organization of this structure was evident, as indicated by the staining of tight junction protein Zonula occludens-1 (ZO-1), podocalyxin, and actin (Figure 7).

As previously mentioned, some reports suggest that laminin polarization plays a crucial role in orienting epithelial and endothelial cells along an apical-basal axis, which is a necessary step for lumen formation. (39, 40). This suggests that stage 4 may present the missing morphogenetic step in which the cords progressively mature into functional, lumenized vessels. In order to confirm this assumption, we evaluated the evolution of cell polarization between the start of stage 3 and the end of stage 4, as well as the maturation of tight junctions, the presence of a lumen and the remodeling of the ECM. Regarding podocalyxin localization, the front view of the structure in both stages revealed that it was two cells thick, which allowed the definition of a top and bottom layer. (Figure 8A). In stage 3, podocalyxin was predominantly expressed at the top cell layer, with no signal detected in the bottom cells or between cell layers. In contrast, during stage 4, when the ECM had completely engulfed the two layers of the cords, podocalyxin was mostly found between the two layers, defining this as the apical side (Figure 8B). This result confirmed our assumption that the edge folding induced apico-basal polarization, with the apical side facing now the interior of the cord structure. This central inner apex of all cord cells is critical for subsequent lumen formation (23) and was consistently found prior to the appearance of a lumen, which gradually emerged in what had now become a microvessel (Figure 2B and Figure 9). Furthermore, lumenization must be accompanied by a consolidation of cell-cell junctions. In our experiments, the organization of ZO-1 clearly changed from cytosolic condensates in the TSEC cells of stage 3 to a prominent localization at the cell-cell regions in stage 4 (Figure 8C and 8D). This transition has been reported elsewhere and was associated with a

response to increased inner pressure during mouse embryo development (24). Finally, a thickening of the structure corresponded to a thickening and reorganization of a BM, aligned by the cells in the direction of the vessels, known to be one the last step of maturation (Figure 8E). Immunofluorescence assays confirmed that collagen IV and laminin were constituents of this thicker BM on top of the structures (Supplementary Figure 5).

All these findings indicate that stage 4 is the maturation stage comparable to those reported in the development of vessels *in vivo*, and that it was achieved spontaneously by cells after the completion of stage 3.

The direction of the vascular structure can be controlled by the initial shape of the guiding edge.
Our simple fabrication method successfully guided the morphogenetic process, promoting the vessel maturation and holding promise for engineering MPS constructs. To further enhance this approach of controlled gelation process and soft ECM edge formation, we next explored different configurations that allow vessel development in a geometry of choice, not limited to a circular shape. A straight line was created by arranging multiple small GelTrex domes in a row. These domes eventually coalesced during gelation, leaving small but visible narrowing between consecutive domes (Figure 9A). To avoid the periodic narrowing, continuous lines were developed by extruding gel manually through a pipette tip (Figure 9B). We also employed a straight support using a polydimethylsiloxane (PDMS) block, a widely used material in microfluidic and MPS applications, against which gel could be deposited while maintaining the outer edge shape (Figure 9C). After 24 hours, for all configurations, cells attached to the edge of the GelTrex similarly to what happened for the domes. After 48 hours, networks of cells were visible in the higher zones of the gel, connecting with the cord formed at the edge, recapitulating the organization shown in the domes in the central and peripheral regions. Finally, after 72 hours, the cords at the edge showed the same behavior as observed in the domes, with stage 4 evident in the zoomed images. This confirms that altering the geometry of the GelTrex deposit does not hinder the self-organized vessel morphogenesis, as long as the pattern obtained by Marangoni flow and the folding-permissive softness of the gel are maintained. It is essential to ensure the proper verticality of the edge, avoiding a flattening on the outside.

Discussion

New models of non-embedded capillaries are needed to better understand the cell mechanisms involved in disease development and preservation of homeostasis. Current models are limited in their ability to imitate discontinued capillaries, such as those found in the liver. In most *in vitro* models of microvessels, perfusable structures are embedded in a thick ECM. Here, we demonstrate an alternative approach where ECs were instructed to spontaneously and autonomously form tubular microvessels, without relying on the support of prefabricated 3D scaffolds or stromal cells (see Summary figure in Supplementary Information). Our methodology is based on patterning the constituents of the basement membrane using the Marangoni effect (29), which has been proven to be a comprehensive guide for vessel morphogenesis. GelTrex was employed as a source of laminin and collagen IV, which are native components of the liver sinusoid BM, found since the early stages of hepatic development (41). Furthermore, GelTrex possesses mechanical properties reminiscent of developmental processes, which favor vasculogenesis and 2D endothelial cord formation (14, 15). Our process involves initiating the formation of patterns at the edge of a dome created by gelation of a sessile droplet. In response to this pattern, LSECs self-organized autonomously, in a sequential manner, to a cord, reshaped their environment, polarized, and ultimately formed a lumen. This entire process is highly structured and occurs across multiple scales, mirroring the morphogenetic nature of in vivo development, leading to the establishment of native quiescence and differentiation states of ECs (42). The anisotropy of our pattern is pivotal for promoting the formation of a long, persistent cord during vasculogenesis. This characteristic prevented the random orientation of cord segments normally observed in conventional 2D assays (12). The patterned ECM initially triggers the cell approach and adhesion stages ,and it appears to be regulated by chemotaxis or haptotaxis, two motility modes known to drive EC morphogenesis (43). Notably, GelTrex contains various growth factors, including VEGF, which presumably attract nearby cells exposed to a diffusive gradient. Across multiple experiments, we consistently observed an attraction distance threshold of approximately 50 µm.

Upon adhesion, cells proliferated and migrated solely along the perimeter, coordinately forming an anisotropic and persistent 1-cell-thick train that rapidly lined the edge. We propose that the ECM pattern was responsible for

collective cell polarization and orientation in this stage. EC morphogenesis mechanisms are indeed significantly affected by shear conditions that can arise from the contractility of the surrounding matrix (44). In aortic ECs, fibrous collagen IV has been reported to direct migration (45), while laminin plays a pivotal role in polarizing other cell types and defining their direction of migration (21). Laminin's plasticity enables long-range cell-cell mechanical communication and alignment in endothelial cells, making it an important ECM factor in vasculogenesis (14, 15). Laminin has also demonstrated a remarkable ability to promote the organization of endothelial segments into cord-like structures and networks. Conversely, when laminin is absent, ECs tend to aggregate into continuous sheets (46). In that last work, the concurrent presence of vascular endothelial growth factors was necessary: removing these factors resulted in the failure of network formation. In our work, laminin and collagen IV were patterned at the edge where the long cell cord formed and the source of growth factors was likely the dome itself. Cells adhering to soft gels can release gel-embedded molecules by exerting pressure on the ECM, making otherwise less accessible soluble factors available in close proximity of contractile cells, through diffusion (47). This is supported by the highly contractile nature of LSECs (37). Then, multicellular cell cords transitioned from 2D to 3D architectures to construct the microvessel. We hypothesize that a gradual shift in cell polarization driven by shear was at play, as suggested in retinal capillaries morphogenesis, for example. Microvessels indeed emerge and organize following different polarization states, triggered by the competing signals of VEGF and shear stress sensed at the focal adhesions (17). Depending on the direction of polarization that they induce, these signals respectively instruct the building of new structures or their remodeling. In our experiment, cells first formed a single peripheral train along the whole perimeter, by what seemed to be preferential division and migration. Only until the entire edge was covered did the proliferation direction change in some locations where cells started to divide perpendicularly and climb up the edge, to form a multicell cord that would then bend the gel and fold it. Planar cell polarization (PCP) could be at play in this change of direction and will need to be further studied. PCP is an important control parameter of endothelial morphogenesis (tubulogenesis and vasculogenesis). It was shown that its regulation by PAR-3 can be simply controlled by fluid flow (48) and that flow-associated shear can remodel the laminin-integrin network (49). Shear stress is known to influence the PCP of endothelial cells, which can even be reversed when shear direction is modified (50). Here, the migration and proliferation of the LSECs on the high-density laminin pattern may have resulted in shear stress signaling, as seen in (51).

Even though the exact mechanism is still not clear, the morphogenetic process involved in the folding stage resembles the formation of invagination furrows, described in tissue development. Although an active mechanism of local apical constriction is capable of generating a wide scale deformation of a whole tissue (52), we rapidly discarded this option here, as we identified no such morphology. However, we identified a long-range 2-step pulling and invaginating process at play in the folding accompanied by a laminin depletion at the basal side of the hinge cell. Similar events were reported in studies of *Drosophila* development. In the embryos, at the wing imaginal discs, localized ECM depletion was identified at the precise moment of a tissue-wide folding (38). During the invagination of the epithelial cells forming the cephalic furrow, it was very recently reported that the infolding serves as a mechanical buffer to release energy increasing due to tissue growth in a confined volume (53). Interestingly, buckling emerged there between two groups of mitotic cells that compressed the central adjacent region and forced it to invaginate sometime after. Interestingly, in our experiments, gel folding also happened between two regions first imposing a lateral stretch to a confined region. Figure 6a shows that slightly thicker clusters of cells were located at both ends of the first folding regions, and we saw it propagate laterally, and close the vessel around the dome in a piecewise manner (Supplementary Figure 6). In our experiments, however, the mechanical instability seems linked to stretching rather than compression and resembles a shear-driven buckling, where a soft sheet of material suffers an out of plane deformation like a transverse shrinking upon extended longitudinal tension (54). Its formal description is complex to explain, but accounts for the appearance of out of plane longitudinal wrinkles or infolds (55). These 2D to 3D transformations usually appear on planar materials with a pre-oriented superficial or inner substructure (usually fibrous), a role that our ECM pattern can play. It is the interplay between this orientation and external stress that defines the direction, length and deformation threshold to start buckling the surface (56). We thus have reasons to believe that the pulling seen by the movements of the beads in Figure 6 is causing the necessary shear behind the subsequent folding. In this aspect, a certain length of persistence seemed necessary for the folding to appear and wrap full cord segments. We reported an approximately periodic repetition of segments of 300 μm that eventually connected and made the full circle vessel. When working with straight GelTrex geometries, on occasions, longer segments emerged at the center of the gel.

Those that were longer than 200 µm had partially folded and buckled the substrate on their central portion, but without being able to fold it completely (Supplementary Figure 7). This apparent length threshold required to deform the soft ECM material seemed related to the amount of shear required to buckle the material, as suggested also by (53) in their *in vivo* experiments. This behavior is most probably due to internal tension building up more prominently when anisotropic (persistent) geometries are found, allowing spatial signaling in the cells forming the cord. This can lead towards the formation of a vessel, as demonstrated with different microfabricated patterns (57).

Lumenogenesis is the last morphogenetic step in *de novo* vessel formation. It clearly required complete wrapping of the multicellular cord by ECM. It has been reported that signaling from the ECM regulates lumen formation by defining polarity in endothelial cells (58). In particular, laminin involves Rac1 and ß1 integrins (59), that orient endothelial cells polarity via Par3 (48). Progression towards lumen formation was confirmed in our experiments by a polarized trafficking of podocalyxin towards the center of the multicellular cord that was formed after folding, establishing this protein as the apical surface, from where the lumen would emerge (19). Then, tight junction protein ZO-1 was recruited at this same region, for lumen maintenance in spite of a probable pressure build up (60). As a sign of maturation, the multicellular cord, that was originally completely wrapped in a very thin GelTrex blanket, was then found to be surrounded by an organized structure of laminin and collagen IV that resembled a thin basement membrane. The evolution observed with electron microscopy between the end of the folding and the later stage after one additional day was striking (Figure 8). Thin, short, wavy fibrous bundles, characteristic of a capillary BM, had been organized and aligned with the direction of the underlying vessel, in a sort of a supramolecular network, characteristic of a liver BM (61), without observing a thicker vessel overall.

In conclusion, through a Marangoni flow-driven patterning of ECM at the edge of a GelTrex dome during its gelation, we triggered a morphogenetic process for LSEC immortalized cells that resembles that of *in vivo* vasculogenesis. Cell migration and proliferation was guided by this pattern to form a 1-cell (1D) train, followed by a multicellular (2D) cord. Cells then folded a thin outer portion of the gel to wrap the cord with ECM. This last morphogenetic step then helped polarize the cells in the interior to open a lumen, forming a vessel. We have described with precision all the stages of this process, to help a further deeper study of the cellular mechanisms and molecular pathways involved. To the best of our knowledge, such a process -involving the anisotropic edge, formation of a EC cord, a wake-like folding and further maturation of the cord- has not been evidenced in the past for endothelial cells, and it is not clear whether this phenomenon (or a similar one) may happen *in vivo* for an endothelium. However, we anticipate positive outcomes from our constructed vessels, the geometry of which can be controlled for integration into MPS to facilitate perfusion.

Materials and Methods

Glass functionalization

Glass coverslips (18 mm, Ted Pella) were sonicated twice in 96% ethanol, followed by a final round in distilled water. In a fume hood, a 2% 3-(Trimethoxysilyl)propyl methacrylate (TMSPMA, Sigma-Aldrich 440159) (v/v) and 1% Acetic Acid (v/v) solution was prepared in absolute ethanol. Each coverslip batch, with a maximum of 15 pieces, was submerged in 10 ml of the solution in a 10 cm petri dish and agitated for 10 minutes at medium speed. Excess solution was discarded, and the coverslips in the petri dish were rinsed with 96% ethanol within the hood. Then they were individually removed from the dish, dipped into clean 96% ethanol, and left to air dry. Functionalized coverslips could be stored in a dust-protected container for one week before their use.

Gelation of GT sessile droplet and cell culture

Functionalized coverslips were UV-sterilized for 30 minutes. Working on an ice bed, the coverslips were placed in a 12 well plate and a 10 µL drop of GelTrex (GT, Gibco, A1413202) was added to each one, without spreading it. The plate was incubated at 37°C with 95% relative humidity for 30 minutes to promote gelation. Following incubation, 1 ml of medium was added to each well to prevent drying before cell seeding. Transformed sinusoidal endothelial cells (TSEC, provided by P. Rautou) were maintained in Dulbecco's Modified Eagle Medium (DMEM,

Gibco 31966021) supplemented with 5% fetal bovine serum (FBS, Gibco, 16000044), 1% Penicillin / Streptomycin (Pen/Strp, Gibco 15140122), 0.4% Amphotericin B (Gibco, 15290026), 1x Endothelial Cell Growth Supplement (EGCS, CliniSciences, 1052-SC). Following trypsinization, cells were counted using a CASY cell counter (OMNI Life Sciences) and cultured at a density of 196 cells/mm^2, ensuring even cell distribution.

Scanning Electron Microscopy

Samples were fixed with 2% glutaraldehyde (Sigma-Aldrich, 340855) in 0.1M cacodylate buffer pH 7.4 for 2 hours at RT. Then samples underwent five 10-minute washes in gentle agitation with 0.1 M cacodylate buffer. Post fixation was performed by incubating samples on ice for 20 minutes in 1% Osmium tetroxide in 0.1M cacodylate buffer. Samples were washed for 5 minutes in gentle agitation with distilled water, five times. Dehydration was achieved by subjecting samples to 10-minute incubations with increasing concentrations of ethanol 50%, 70%, 95%, 100%, absolute ethanol. Final drying was performed through evaporation of hexamethyldisilazane (HMDS), first with a 10 minute incubation of HDMS 50% in absolute ethanol, followed by two incubations of HMDS 100%. The dried samples were mounted onto sample holders and coated with platinum before being imaged with a Cryo-SEM GeminizeM500 using immersion lens and SE2 detectors.

Characterization of GT droplets

For density evaluation, network filling factor, obtained from SEM images, was defined as the ratio of the area occupied by the ECM to the total area of the image. Regarding gel mechanics, GT droplets were immersed in complete medium and nanoindented (Piuma system, Optics11). Measurements were obtained over the course of several dome radii. Estimation of the material's Young's modulus was performed using a Hertz model fitting.

Live imaging

35 mm glass-bottomed petri dishes (World Precision Instruments, FD35-100) were functionalized with TMSPMA as previously described. Subsequently, a 10 µL GT droplet was placed in each dish, gelated and cultured as described in 2.2. Phase contrast microscopy images were acquired every 10 minutes for 5 days using a BioStation IM-Q (Nikon).

For live fluorescence microscopy, FluoSpheres™ Carboxylate-Modified Microspheres (Invitrogen, F8786) (dilution 1:1000 in DMEM) were added to the GelTrex prior gelation (final GT concentration 95%). Additionally, cells were incubated with CellMask™ Green Actin Tracking Stain (Invitrogen, A57243) (dilution 1:1000 in starving medium) for 30 minutes at 37°C. Nuclei were stained with Hoechst (Invitrogen, 33342) (diluted to 1 ug/mL) for 10 minutes at RT. Image acquisition was performed using a Zeiss LSM 980 Inverted confocal microscope.

Immunofluorescence

Samples were fixed for 15 minutes at 37 °C with 0.4% Paraformaldehyde (PFA. Sigma-Aldrich, P6148) in Phosphate-buffered saline (PBS, Sigma-Aldrich, P3813), permeabilized with 0.1% Triton X-100 (Sigma-Aldrich, X100) in PBS for 10 min at RT, in agitation; and blocked with 10% horse serum (HS, Sigma-Aldrich, H1270) for 1 hour. After blocking, primary antibodies corresponding to Laminin 111 (Novus Biologicals, NB300-144SS) (1:1000 dilution), Collagen IV (Novus Biologicals, NB120-6586SS and NBP1-26549) (1:500 dilution), Podocalyxin (R&D systems, AF1556) (1:250 dilution), and ZO-1 (Invitrogen, 10342463)(1:50 dilution) were diluted in blocking buffer and incubated at 4◦C overnight. Then samples were incubated for 2 hours with second antibodies: goat anti-rabbit (Alexa Fluor 633, 1:500), donkey anti-goat (Alexa Fluor 594, 1:400). For F-actin staining, samples were incubated for 45 minutes with Alexa Fluor™ 488 Phalloidin (Invitrogen, A12379). Nuclear staining was performed through incubation of 4′,6-Diamidino-2-phenylindole dihydrochloride (DAPI, Sigma-Aldrich, D8417) diluted 1:250 in PBS. Samples were imaged with a Zeiss LSM 980 Inverted confocal microscope using an oil-immersed objective (63x) with a 0.5 µm step for Z-stack acquisition.

Quantification and Statistical analysis

Image analysis was performed using Fiji image analysis software (62). If not stated otherwise, data are presented as mean ± SD from at least two independent experiments. Graphs were generated through the Matplotlib graphic package (63). Statistical analysis to assess differences among experimental groups was

performed using a t-student test in Python's SciPy sub-package (64). A significance level of P<0.05 was considered significant and notation is as follows: P<0.05 "*", P<0.01 "**", P<0.001 "***" , P<0.0001 "****".

Acknowledgments
Ana Ximena Monroy-Romero conducted this study to fulfill the requirements of Programa de Doctorado en Ciencias Biomédicas of Universidad Nacional Autónoma de México, and received a doctoral scholarship from Consejo Nacional de Humanidades, Ciencias y Tecnologías (1004395). The authors are thankful to Michaël Trichet and Alexis Canette from the IBPS electron microscopy core facility and France Lam from the IBPS microscopy core facility (Sorbonne-Université, CNRS) for their support in imaging. Special thanks to Pierre Emmanuel Rautou for kindly providing the TSEC cell line and to him and his team for engaging in project discussions. We also thank Marina Macías-Silva for providing the TMNK-1 cell line. We extend our gratitude to Benoit Ladoux, René Marc Mège and Sushil Dubey for providing us access to the Nikon BioStation and for their continuous support in this project. Lastly, we express our gratitude to Michel Labouesse and his team at IBPS for hosting us in their laboratory. The team was funded by the i-Bio initiative and this work was partially supported by a DIM ELICIT's grant from Région Ile-de-France.

References

1. C. A. Dessalles, C. Ramón-Lozano, A. Babataheri, A. I. Barakat, Luminal flow actuation generates coupled shear and strain in a microvessel-on-chip. *Biofabrication* 14 (2021).
2. W. J. Polacheck, M. L. Kutys, J. B. Tefft, C. S. Chen, Microfabricated blood vessels for modeling the vascular transport barrier. *Nat. Protoc.* 14, 1425–1454 (2019).
3. D.-H. T. Nguyen, *et al.*, A biomimetic pancreatic cancer on-chip reveals endothelial ablation via ALK7 signaling. *Sci Adv* 5, eaav6789 (2019).
4. A. Chhabra, *et al.*, A vascularized model of the human liver mimics regenerative responses. *Proc. Natl. Acad. Sci. U. S. A.* 119, e2115867119 (2022).
5. V. van Duinen, *et al.*, Perfused 3D angiogenic sprouting in a high-throughput in vitro platform. *Angiogenesis* 22, 157–165 (2018).
6. K. Haase, G. S. Offeddu, M. R. Gillrie, R. D. Kamm, Endothelial Regulation of Drug Transport in a 3D Vascularized Tumor Model. *Adv. Funct. Mater.* 30 (2020).
7. , The vascular system: An overview of structure and function. *J. Pharmacol. Toxicol. Methods* 44, 333–340 (2000).
8. K. K. Sørensen, J. Simon-Santamaria, R. S. McCuskey, B. Smedsrød, Liver Sinusoidal Endothelial Cells. *Compr. Physiol.* 5, 1751–1774 (2015).
9. E. Wisse, R. B. De Zanger, K. Charels, P. Van Der Smissen, R. S. McCuskey, The liver sieve: considerations concerning the structure and function of endothelial fenestrae, the sinusoidal wall and the space of Disse. *Hepatology* 5, 683–692 (1985).
10. S. Soydemir, O. Comella, D. Abdelmottaleb, J. Pritchett, Does Mechanocrine Signaling by Liver Sinusoidal Endothelial Cells Offer New Opportunities for the Development of Anti-fibrotics? *Front. Med.* 6, 312 (2019).
11. E. Felli, *et al.*, Mechanobiology of portal hypertension. *JHEP Rep.* 5, 100869 (2023).
12. Y. Kubota, H. K. Kleinman, G. R. Martin, T. J. Lawley, Role of laminin and basement membrane in the morphological differentiation of human endothelial cells into capillary-like structures. *J. Cell Biol.* 107, 1589–1598 (1988).
13. B. Strilić, *et al.*, The molecular basis of vascular lumen formation in the developing mouse aorta. *Dev. Cell* 17, 505–515 (2009).
14. M. Ouyang, *et al.*, Sensing Traction Force on the Matrix Induces Cell-Cell Distant Mechanical Communications for Self-Assembly. *ACS Biomater Sci Eng* 6, 5833–5848 (2020).
15. D. Rüdiger, *et al.*, Cell-Based Strain Remodeling of a Nonfibrous Matrix as an Organizing Principle for Vasculogenesis. *Cell Rep.* 32, 108015 (2020).
16. F. le Noble, *et al.*, Flow regulates arterial-venous differentiation in the chick embryo yolk sac. *Development* 131, 361–375 (2004).
17. P. Barbacena, *et al.*, Competition for endothelial cell polarity drives vascular morphogenesis in the mouse retina. *Dev. Cell* 57, 2321–2333.e9 (2022).

18. P. Rajendran, *et al.*, The vascular endothelium and human diseases. *Int. J. Biol. Sci.* 9, 1057–1069 (2013).
19. M. Richards, C. Hetheridge, H. Mellor, The Formin FMNL3 Controls Early Apical Specification in Endothelial Cells by Regulating the Polarized Trafficking of Podocalyxin. *Curr. Biol.* 25, 2325–2331 (2015).
20. C. R. Francis, E. J. Kushner, Trafficking in blood vessel development. *Angiogenesis* 25, 291–305 (2022).
21. K. S. Matlin, S.-M. Myllymäki, A. Manninen, Laminins in Epithelial Cell Polarization: Old Questions in Search of New Answers. *Cold Spring Harb. Perspect. Biol.* 9 (2017).
22. J. L. Lee, C. H. Streuli, Integrins and epithelial cell polarity. *J. Cell Sci.* 127, 3217–3225 (2014).
23. A. Datta, D. M. Bryant, K. E. Mostov, Molecular regulation of lumen morphogenesis. *Curr. Biol.* 21, R126–36 (2011).
24. N. Kinoshita, *et al.*, Force-dependent remodeling of cytoplasmic ZO-1 condensates contributes to cell-cell adhesion through enhancing tight junctions. *iScience* 25, 103846 (2022).
25. V. Gebala, R. Collins, I. Geudens, L.-K. Phng, H. Gerhardt, Blood flow drives lumen formation by inverse membrane blebbing during angiogenesis in vivo. *Nat. Cell Biol.* 18, 443–450 (2016).
26. D. B. Camasão, D. Mantovani, The mechanical characterization of blood vessels and their substitutes in the continuous quest for physiological-relevant performances. A critical review. *Mater Today Bio* 10, 100106 (2021).
27. J. Poisson, *et al.*, Liver sinusoidal endothelial cells: Physiology and role in liver diseases. *J. Hepatol.* 66, 212–227 (2017).
28. P. Tracqui, P. Namy, J. Ohayon, “In vitro tubulogenesis of endothelial cells: Analysis of a bifurcation process controlled by a mechanical switch” in *Mathematical Modeling of Biological Systems*, (Birkhäuser Boston, 2007), pp. 47–57.
29. B. A. Nerger, P.-T. Brun, C. M. Nelson, Marangoni flows drive the alignment of fibrillar cell-laden hydrogels. *Sci Adv* 6, eaaz7748 (2020).
30. C. M. Nelson, *et al.*, Emergent patterns of growth controlled by multicellular form and mechanics. *Proc. Natl. Acad. Sci. U. S. A.* 102, 11594–11599 (2005).
31. S. S. Soofi, J. A. Last, S. J. Liliensiek, P. F. Nealey, C. J. Murphy, The elastic modulus of Matrigel as determined by atomic force microscopy. *J. Struct. Biol.* 167, 216–219 (2009).
32. R. Long, M. S. Hall, M. Wu, C.-Y. Hui, Effects of gel thickness on microscopic indentation measurements of gel modulus. *Biophys. J.* 101, 643–650 (2011).
33. Y. Lei, O. F. Zouani, M. Rémy, C. Ayela, M.-C. Durrieu, Geometrical microfeature cues for directing tubulogenesis of endothelial cells. *PLoS One* 7, e41163 (2012).
34. R. C. Huebert, *et al.*, Immortalized liver endothelial cells: a cell culture model for studies of motility and angiogenesis. *Lab. Invest.* 90, 1770–1781 (2010).
35. A. Baiocchini, *et al.*, Liver sinusoidal endothelial cells (LSECs) modifications in patients with chronic hepatitis C. *Sci. Rep.* 9, 8760 (2019).
36. T. Matsumura, *et al.*, Establishment of an immortalized human-liver endothelial cell line with SV40T and hTERT. *Transplantation* 77, 1357–1365 (2004).
37. H. Zhao, *et al.*, Bi-content micro-collagen chip provides contractility-based biomechanical readout for phenotypic drug screening with expanded and profiled targets. *Lab Chip* 15, 3481–3494 (2015).
38. L. Sui, *et al.*, Differential lateral and basal tension drive folding of Drosophila wing discs through two distinct mechanisms. *Nat. Commun.* 9, 4620 (2018).
39. K. S. Matlin, S.-M. Myllymäki, A. Manninen, Laminins in Epithelial Cell Polarization: Old Questions in Search of New Answers. *Cold Spring Harb. Perspect. Biol.* 9 (2017).
40. J. L. Lee, C. H. Streuli, Integrins and epithelial cell polarity. *J. Cell Sci.* 127, 3217–3225 (2014).
41. A. Couvelard, *et al.*, Structural and functional differentiation of sinusoidal endothelial cells during liver organogenesis in humans. *Blood* 87, 4568–4580 (1996).
42. T. Korff, H. G. Augustin, Integration of endothelial cells in multicellular spheroids prevents apoptosis and induces differentiation. *J. Cell Biol.* 143, 1341–1352 (1998).
43. J. T. Daub, R. M. H. Merks, A cell-based model of extracellular-matrix-guided endothelial cell migration during angiogenesis. *Bull. Math. Biol.* 75, 1377–1399 (2013).
44. S. Hsu, R. Thakar, D. Liepmann, S. Li, Effects of shear stress on endothelial cell haptotaxis on micropatterned surfaces. *Biochem. Biophys. Res. Commun.* 337, 401–409 (2005).
45. T. J. Herbst, J. B. McCarthy, E. C. Tsilibary, L. T. Furcht, Differential effects of laminin, intact type IV collagen, and specific domains of type IV collagen on endothelial cell adhesion and migration. *J. Cell Biol.* 106, 1365–1373 (1988).
46. K. Stamati, J. V. Priestley, V. Mudera, U. Cheema, Laminin promotes vascular network formation in 3D in vitro collagen scaffolds by regulating VEGF uptake. *Exp. Cell Res.* 327, 68–77 (2014).

47. K. Y. Lee, M. C. Peters, K. W. Anderson, D. J. Mooney, Controlled growth factor release from synthetic extracellular matrices. *Nature* 408, 998–1000 (2000).
48. T. Hikita, *et al.*, PAR-3 controls endothelial planar polarity and vascular inflammation under laminar flow. *EMBO Rep.* 19 (2018).
49. E. P. Béguin, *et al.*, Flow-induced Reorganization of Laminin-integrin Networks Within the Endothelial Basement Membrane Uncovered by Proteomics. *Mol. Cell. Proteomics* 19, 1179–1192 (2020).
50. S. McCue, *et al.*, Shear stress regulates forward and reverse planar cell polarity of vascular endothelium in vivo and in vitro. *Circ. Res.* 98, 939–946 (2006).
51. J. Di Russo, *et al.*, Endothelial basement membrane laminin 511 is essential for shear stress response. *EMBO J.* 36, 183–201 (2017).
52. B. He, K. Doubrovinski, O. Polyakov, E. Wieschaus, Apical constriction drives tissue-scale hydrodynamic flow to mediate cell elongation. *Nature* 508, 392–396 (2014).
53. B. C. Vellutini, *et al.*, Pre-patterned epithelial invagination prevents mechanical instability during fly gastrulation. *bioRxiv* (2023) https:/doi.org/10.1101/2023.03.30.534554.
54. J. Zhu, X. Zhang, T. Wierzbicki, Stretch-induced wrinkling of highly orthotropic thin films. *Int. J. Solids Struct.* 139-140, 238–249 (2018).
55. J. Beter, *et al.*, The Tension-Twist Coupling Mechanism in Flexible Composites: A Systematic Study Based on Tailored Laminate Structures Using a Novel Test Device. *Polymers* 12 (2020).
56. Q. Wang, X. Zhao, A three-dimensional phase diagram of growth-induced surface instabilities. *Sci. Rep.* 5, 8887 (2015).
57. N. C. Rivron, *et al.*, Tissue deformation spatially modulates VEGF signaling and angiogenesis. *Proc. Natl. Acad. Sci. U. S. A.* 109, 6886–6891 (2012).
58. A. C. Zovein, *et al.*, Beta1 integrin establishes endothelial cell polarity and arteriolar lumen formation via a Par3-dependent mechanism. *Dev. Cell* 18, 39–51 (2010).
59. W. Yu, *et al.*, Beta1-integrin orients epithelial polarity via Rac1 and laminin. *Mol. Biol. Cell* 16, 433–445 (2005).
60. A. Szymborska, H. Gerhardt, Hold Me, but Not Too Tight-Endothelial Cell-Cell Junctions in Angiogenesis. *Cold Spring Harb. Perspect. Biol.* 10 (2018).
61. K. M. Mak, R. Mei, Basement Membrane Type IV Collagen and Laminin: An Overview of Their Biology and Value as Fibrosis Biomarkers of Liver Disease. *Anat. Rec.* 300, 1371–1390 (2017).
62. J. Schindelin, *et al.*, Fiji: an open-source platform for biological-image analysis. *Nat. Methods* 9, 676–682 (2012).
63. J. D. Hunter, Matplotlib: A 2D Graphics Environment. *Comput. Sci. Eng.* 9, 90–95 (2007).
64. P. Virtanen, *et al.*, SciPy 1.0: fundamental algorithms for scientific computing in Python. *Nat. Methods* 17, 261–272 (2020).

Figures and Tables

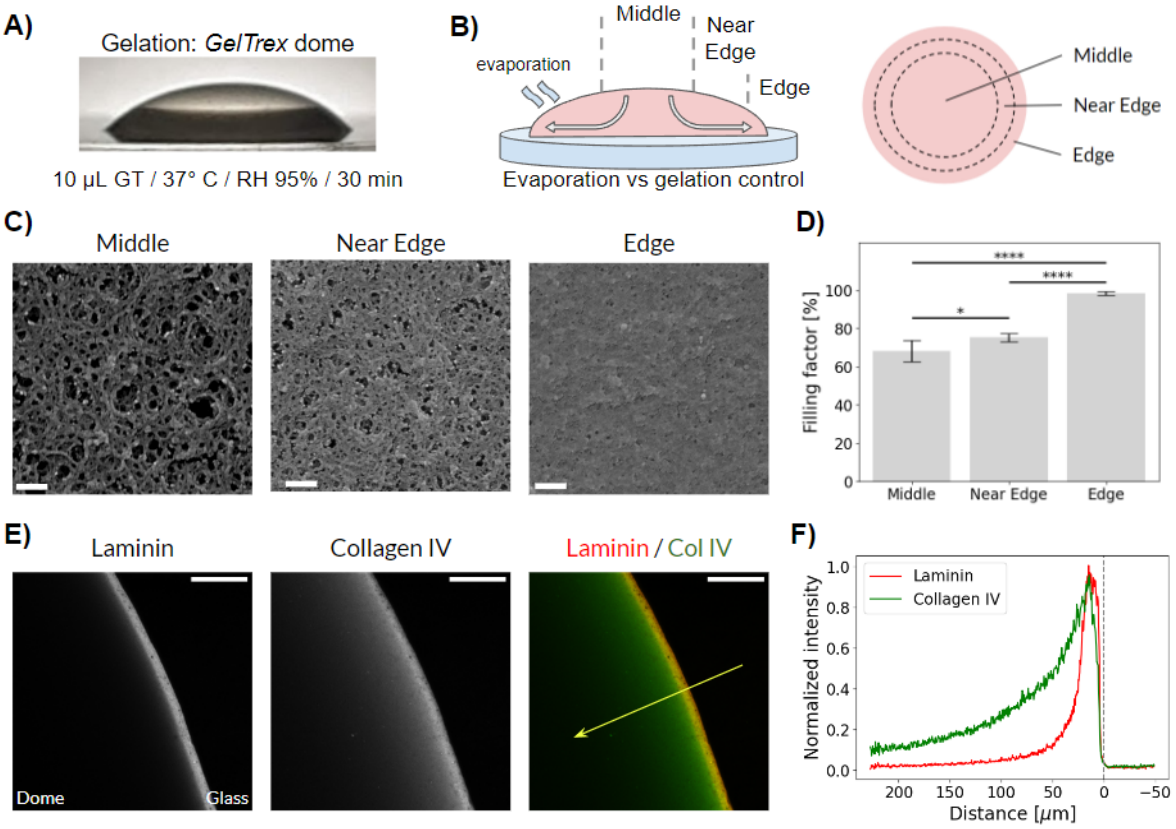

Figure 1. Gelation of a sessile droplet of GelTrex defines a dome with density gradient ending in a ring pattern of laminin at the edge. A) Transversal-view brightfield image of a gelated GelTrex dome. B) Schematic of the evaporation during gelation generating a Marangoni flow, leading to the generation of three specific concentric zones in the dome: middle, near edge and edge. C) Micrographs from scanning electron microscopy of the ECM from three different zones of the dome after gelation, demonstrating higher density towards the edge. Scale bars = 100 nm. D) Comparison of computed ECM filling factor in the three zones (n=3 per group). E) Confocal Z projections of dome edge stained for laminin and collagen IV showing a thin ring-like pattern characteristic of Marangoni-derived pattern. Scale bars = 100 µm. F) Intensity profiles of transversal lines pointing inside the dome (yellow arrow) traced for laminin and collagen IV. Average profiles for 4 samples for each stainings; distance 0 µm corresponding to the edge of the dome ("*" P<0.05, "****" P<0.0001).

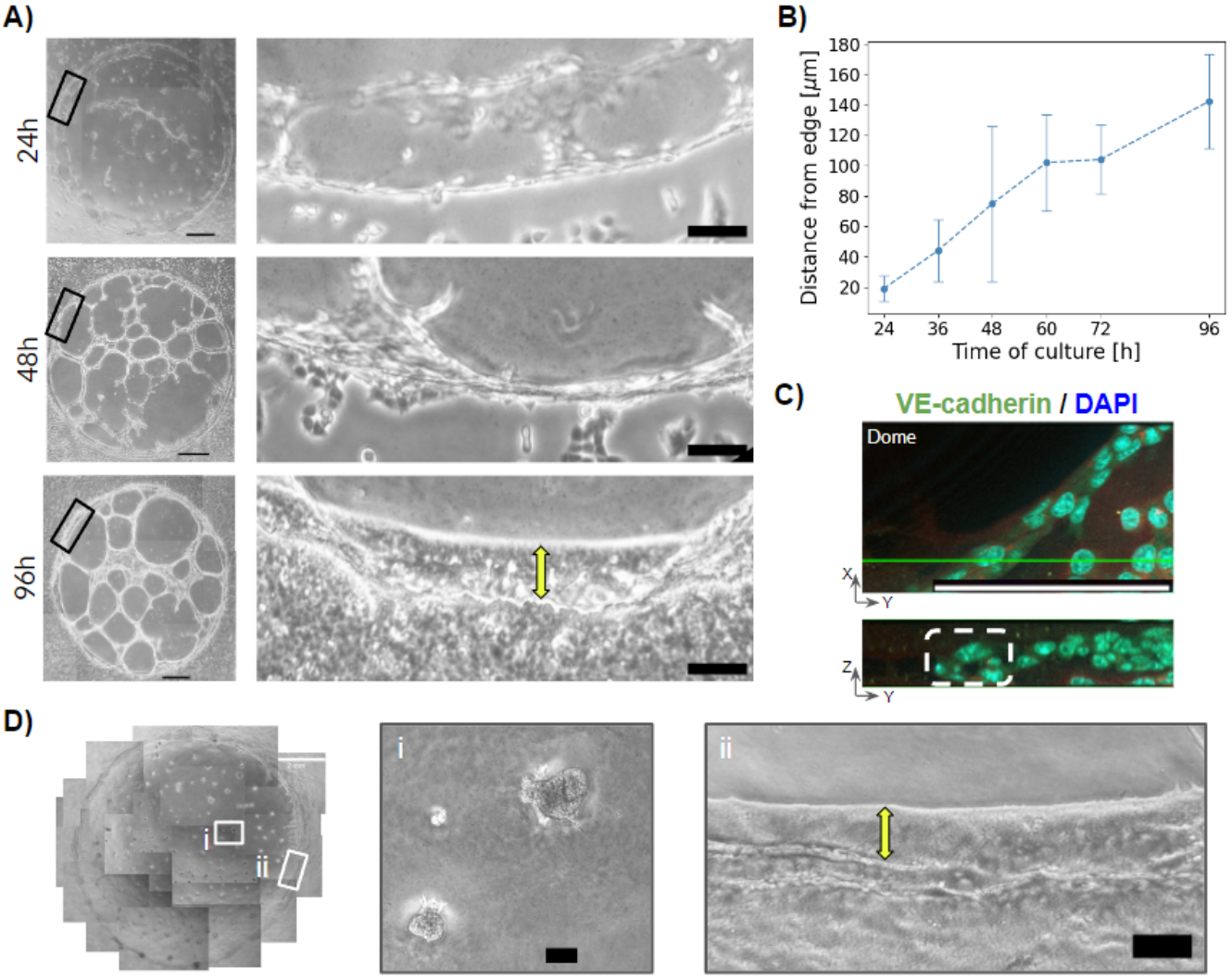

Figure 2. Endothelial cells self organize in a lumenized structure following the ring pattern at the edge of a GelTrex dome. A) Top-view brightfield images of TSECs cultured on GelTrex domes at 24h, 48h and 96h. Left side pictures allow to visualize the whole dome with networks forming at the middle as in conventional vasculogenesis assay, scale bar = 500 µm. Black rectangles indicate the zoomed region shown beside, focusing on the edge and showing the progression of the organization, scale bar = 100 µm. B) Distance from the edge of a front formed during the cell organization was measured, showing an increase in width. n = 3 C) Confocal image of the structure formed at the edge of a GT dome stained for VE-cadherin, scale bar = 100 µm. Below, transversal cross-section showing a tubular structure with a lumen (lined white square). D) Top-view brightfield image of second possible structural endpoint of TSECs cultured for 72h on a GelTrex dome, scale bar = 2 mm. Cells organize in the center in networks as in panel A) but eventually detached from their ends and tangled up into 3D aggregates of various sizes shown zoomed in i). However, the organization at the edge remained as that of the panel A), shown zoomed in ii) with a second front separated from the edge of the dome.

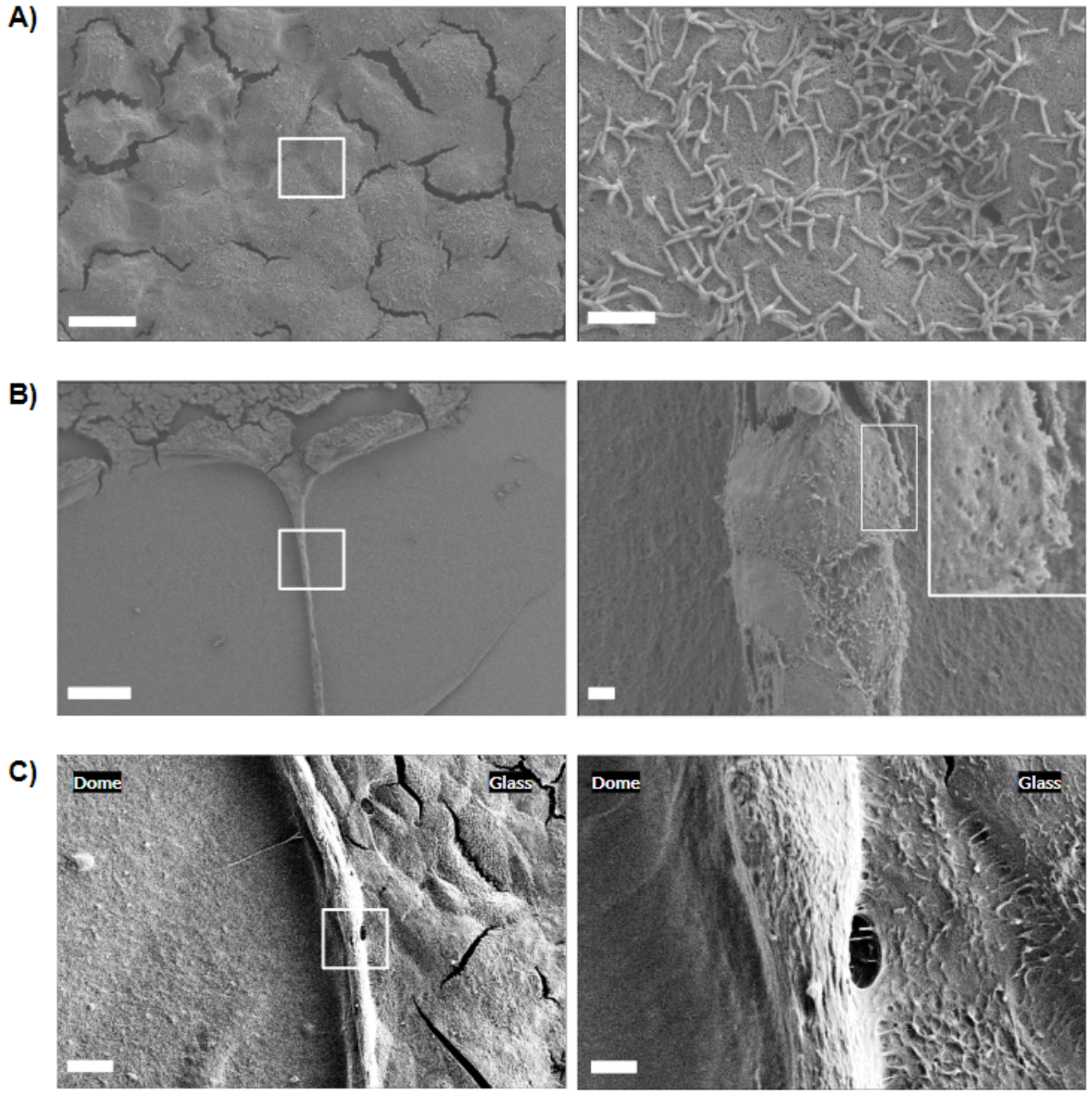

Figure 3 Culture on GelTrex domes guide endothelial cells into three different morphogenetic multicellular shapes depending on their localization. Representative micrographs from scanning electron microscopy of TSECs cultured for 96 hours on a GelTrex dome. A) Cells attached to the glass proliferated and formed a monolayer characterized by the cobblestone morphology, scale bar = 10 µm . Zoomed region shows the presence of cilia structure on the cells, scale bar = 1 µm . B) On the dome, cells are organized in multicellular cords that are connected to the edge, scale bar = 100 µm. Zoomed region shows loose cell-cell junctions and large openings, scale bar = 2 µm. C) Cells at the edge (dome to the left, glass to the right) organize in a cord of elongated cells, scale bar = 10 µm. Zoomed region shows that the cord appears to be covered by a thin ECM-like coating, scale bar = 2 µm.

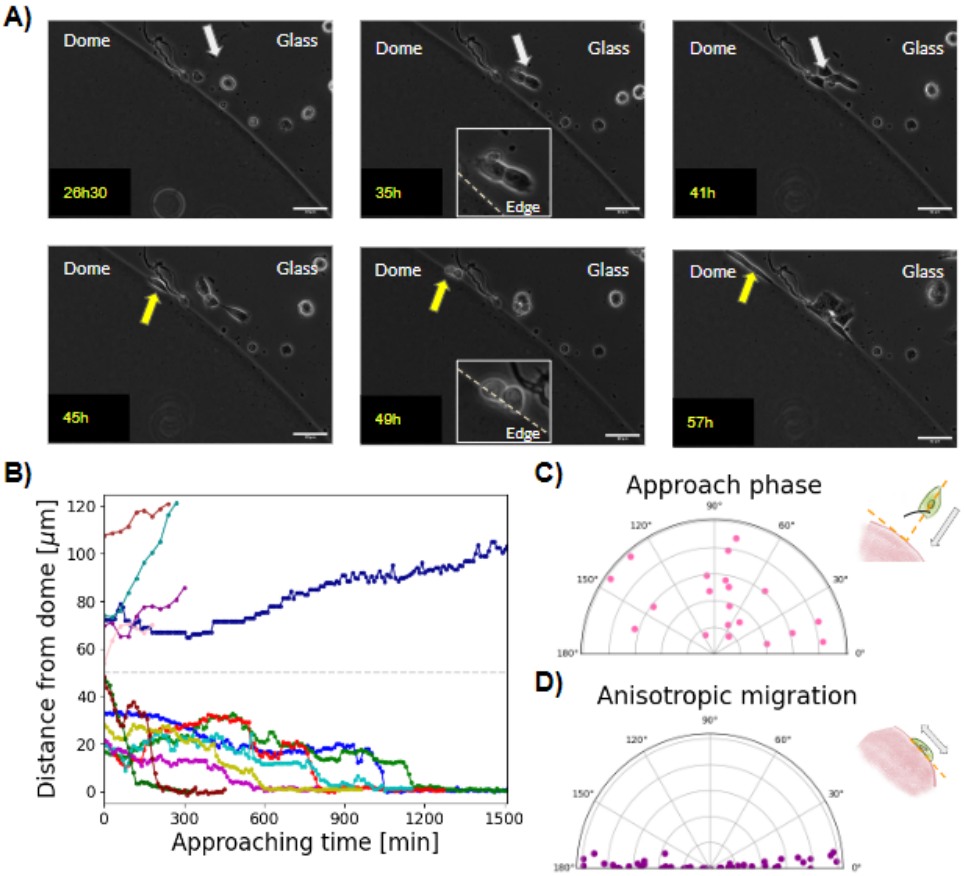

Figure 4. First stage of endothelial organization is characterized by migration towards the dome and preferential adhesion and proliferation along the edge. A) Micrographs from bright field microscopy (frames from MovieS1) showing the progression of organization at the edge. First cells migrate towards the dome (white arrow, top line) and proliferate with no particular direction (top). After they have reached the edge, they modify their direction of migration and move along the edge (yellow arrows, bottom line) and their proliferation follows the direction of the edge. Scale bar = 50 μm B) Displacement of individual cells followed in time. Minute 0 of approaching time corresponds to the beginning of the migration of the cells. Cells at a maximum distance of 50 μm (gray line) migrated towards the dome whereas those at a higher distance either migrated away from the dome or maintained their distance from the edge. n = 13 cells. C) and D) The angle between the cell migration and tangents to the edge was measured, both for the approach phase and after they adhered to the edge. n = 8 cells.

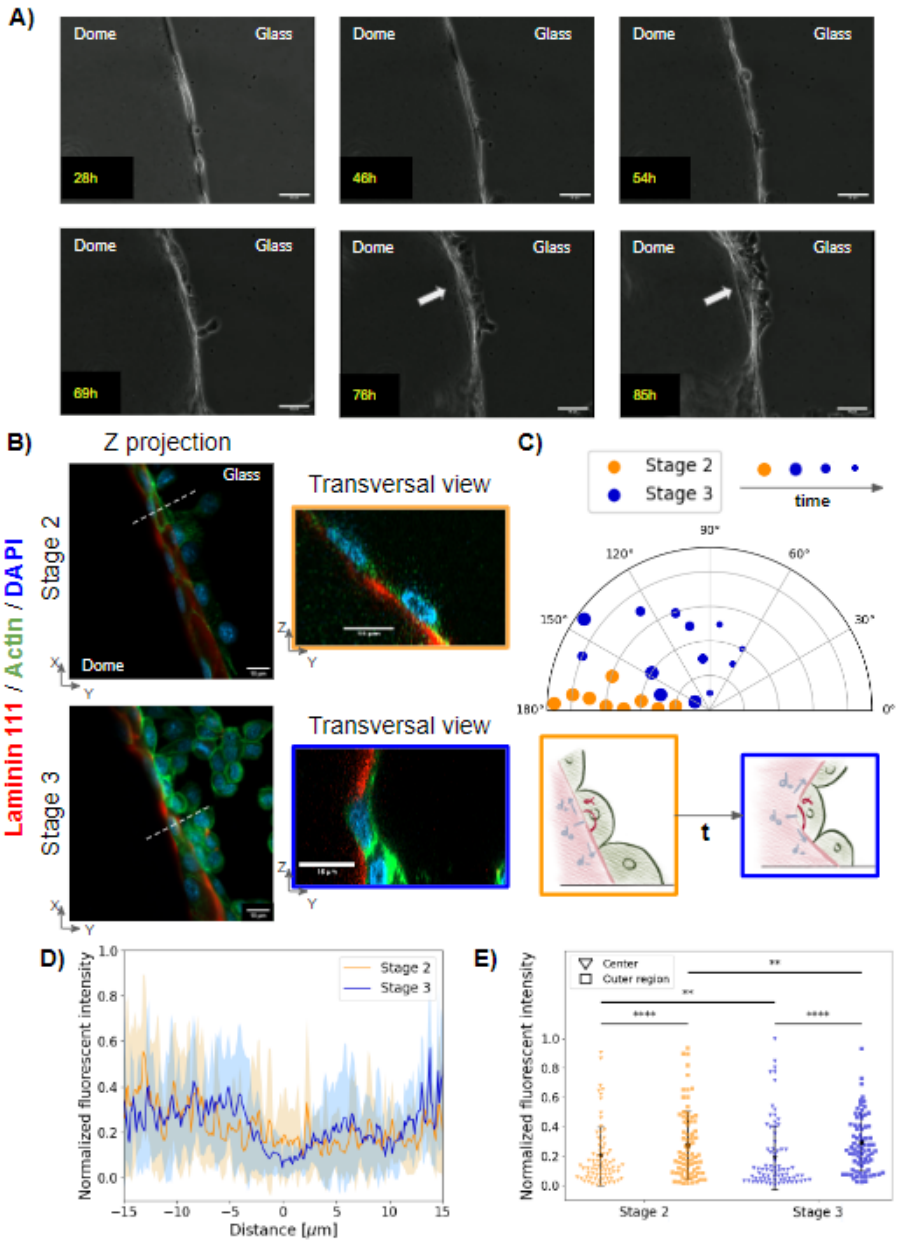

Figure 5. Progression of the thin cell line into a multicellular cord structure and ECM edge folding. A) Micrographs from bright field microscopy (frames from Movie S2 and Movie S3) showing the progression of organization at the edge. Top line: cells at the edge continue to migrate and proliferate on it until they have cored the whole circumference with a thin cord of cells. Bottom line: Cord becomes thicker shown by the appearance of a white front over already existing cells. This white cord starts to separate from the dome as shown by the white arrow. Scale bar = 50 µm. B) Two stages of the organization were identified thanks to staining against laminin (to identify the dome) and with phalloidin and DAPI (to identify the cells). Z projections of both stage 2 and 3 show cells following the dome edge. Scale bar = 15 µm. However transversal cross-sections show a difference between stages. In stage 2, cells are going on the dome following a straight line, while in stage 3 the dome is being folded with a decrease in intensity in the center of the folding. Scale bar = 15 µm. C) The angle alpha, centered in d0 as shown in the schematic, was measured for samples in stage 2 and stage 3. Size of dots decreases for samples with longer times of culture. n= 3 and 5 per group D) Profiles of the border of the dome were measured for the signal of laminin in stage 2 and 3. A decrease in intensity can be seen in the center region (0 µm corresponds to d0 as shown in the schematic in C) n= 3 and 5 per group. E) Comparison of normalized intensity at the center and outer region (d-). n= 3 and 5 per group. ("**" P<0.01, "****" P<0.0001)

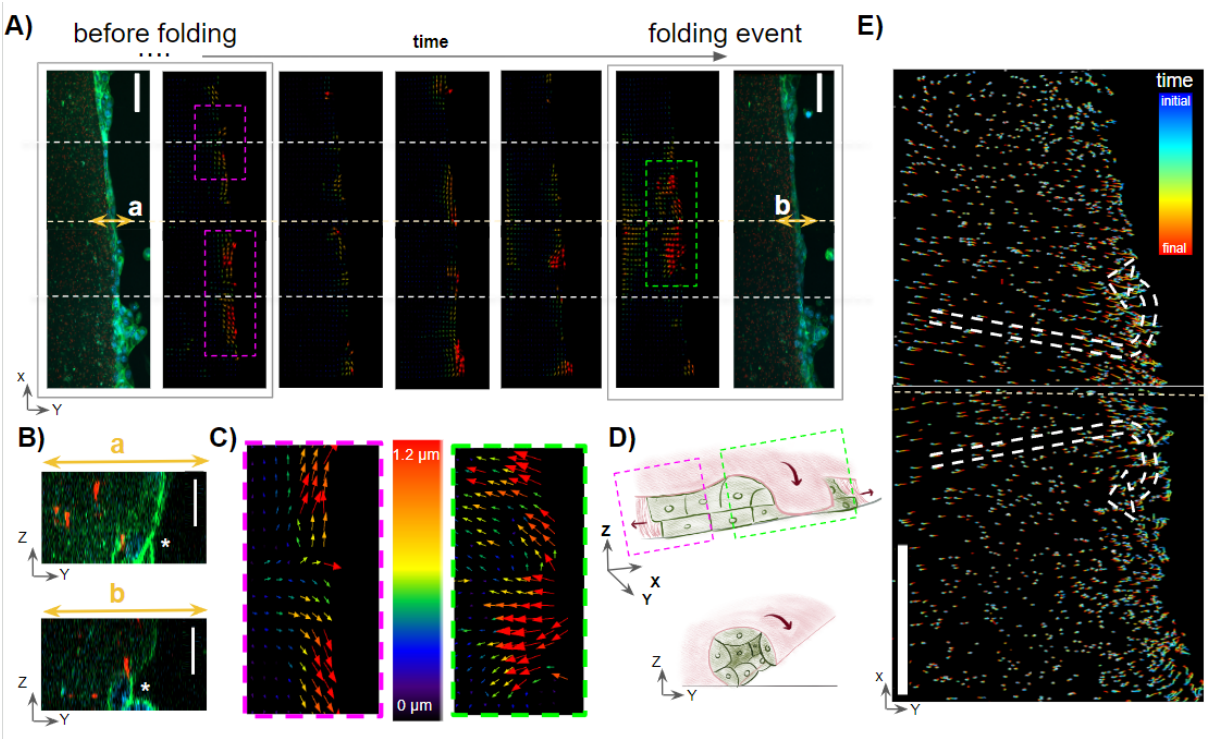

Figure 6. The deformation of the gel in opposite directions along the edge axis initiates folding in a wave-like manner. A) Characteristic temporal evolution of a folding process. Confocal images show the edge of a dome with embedded fluorescent beads and the cord organization of the endothelial cells. Scale bar = 50 µm. In regions marked as ‘a’ and ‘b’, transverse sections were obtained and displayed in B), illustrating the progression of the fold. Scale bar = 15 µm. Among the photos are the displacement maps of the beads every 30 minutes. C) A magnified view is provided for one of the regions displaying bead displacement before folding (highlighted in purple) and the central bead displacement corresponding to the folding event (highlighted in green). The color scale indicates the length of displacement. D) Schematic representation of folding behavior. Cells deform the gel alongside the edge axis in opposite directions which leads to the in-between gel part to move in a wake-live manner. The front in the green box advances to the point where it creates a distinctive crest or "lip" at the wave's front creating a folding effect, similar to a breaking wave. The cord of cells is then located in the “tube” of the wave that progresses to close as time passes, covering them with ECM. E) The comprehensive trajectory of each individual bead throughout the experiment is presented. Maximum displacement is observed in the central region of the field, coinciding with the folding event. Blue is the initial starting point of measurement and red indicates the final location. Opposite global directions are clearly visible between the edge and inner regions. Scale bar: 100 µm.

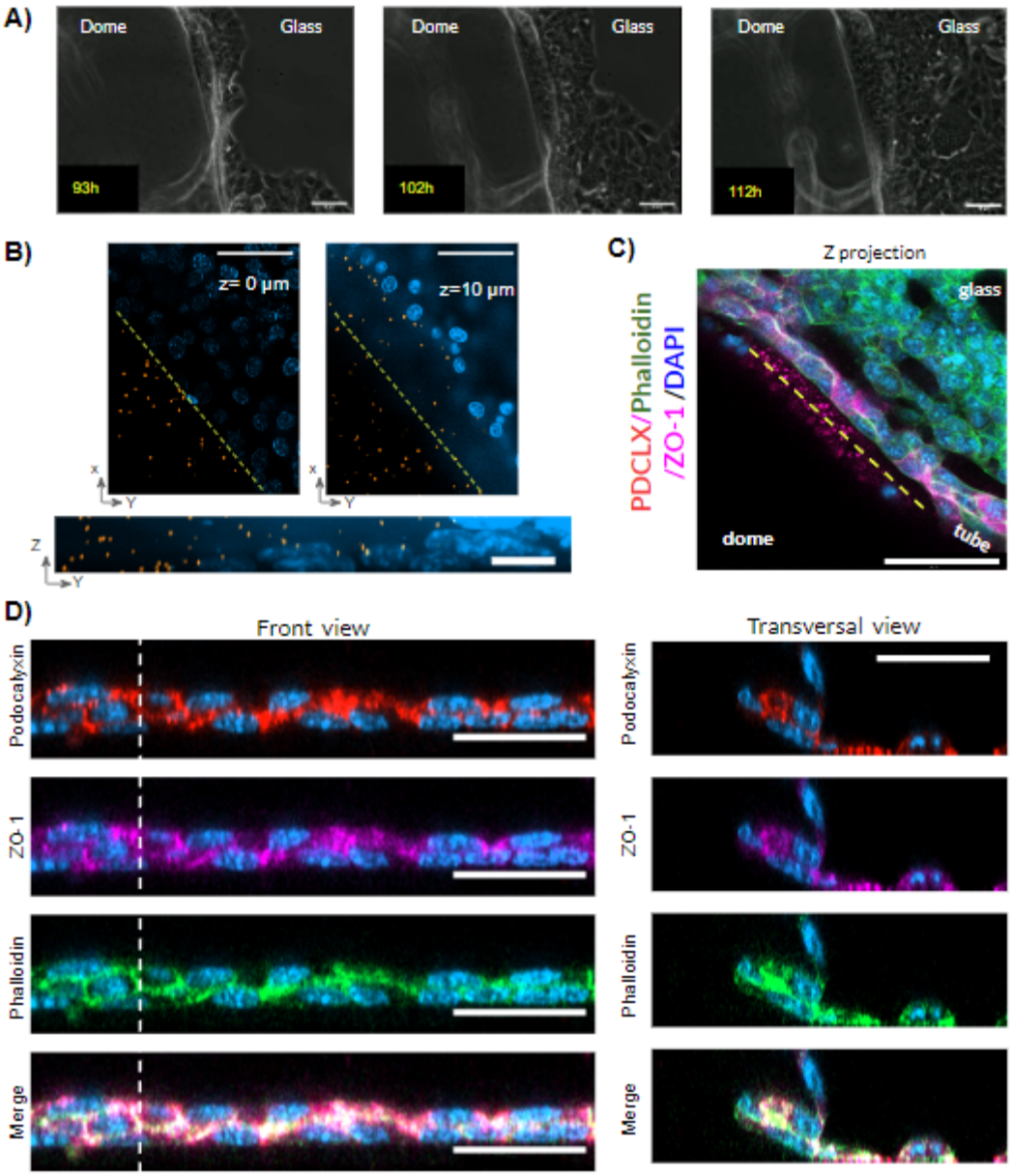

Figure 7. Final stage of organization includes closing of the fold and covering the cells closer to the dome, both cord and monolayer, with gel. A) Micrographs from bright field microscopy (frames from Movie S4) showing the progression of organization at the edge. The cord observed in stage 3 continues to move away from the original edge of the dome. Scale bar = 50 µm. B) Domes with fluorescent beads embedded were used to visualize further deformation of the dome. By looking at different heights of the samples we could observe that the front of the beads, indicating the edge of the dome, were moving further from the edge as height increased, scale bar = 50 µm. Furthermore, the transversal cross-section showed beads over nuclei staining and not in between them, showing that cells were covered by the gel. Scale bar = 10 µm C) Confocal images against Podocalyxin and ZO-1 with phalloidin staining showed that the structure at the edge of the dome presented cells organized in a weaved manner. It also shows a difference in protein expression between the tubular structure and the monolayer on glass. In order to corroborate this organization, side view of the structure (following yellow line) was observed. Scale bar = 25 µm D) Side view of structures at the edge that show a zigzag organization of the cells. The transverse cross section of the structure showed that the folding had finished with a closed structure as result, scale bar = 25 µm.

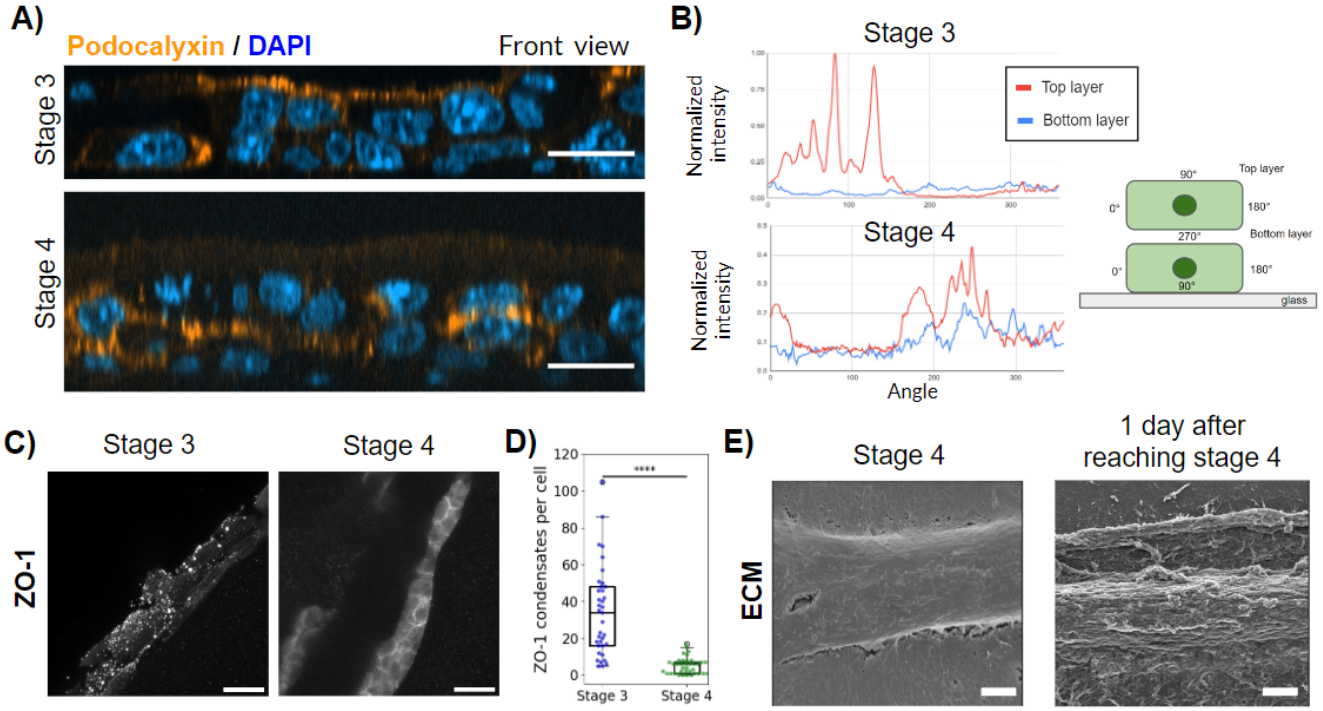

Figure 8. Complete folding of the GT dome promotes the maturation of a lumenized vascular structure. A) Front view micrographs of capillary-size structure stained for Podocalyxin (PDCLX) during stages 3 and 4. Scale bar = 15 µm B) Cell periphery intensity profiles were obtained for pairs of cells (one in the top layer and one in the bottom layer, as shown in the schematic). Normalized intensity as function of the angle shows a change in localization from the top part of the structure (angles 0°- 180° in red) to in between layers (angles 180° - 360°, red and blue) can be seen. n = 2 C) Confocal micrographs show the expression of ZO-1 in stage 3, as intracellular condensates, and stage 4, localized at cell-cell interfaces in the vascular structures. Scale bar = 15 µm D) Number of ZO-1 condensates per cell in the structure decreases in stage 4 compared to stage 3. n = 2 E) Scanning electron microscopy (SEM) micrographs of vascular structures in stage 4 with a thin ECM layer over it as well as structures with one more day of culture after stage 4 with a thick and organized ECM layer over the structure. Scale bar = 2 µm

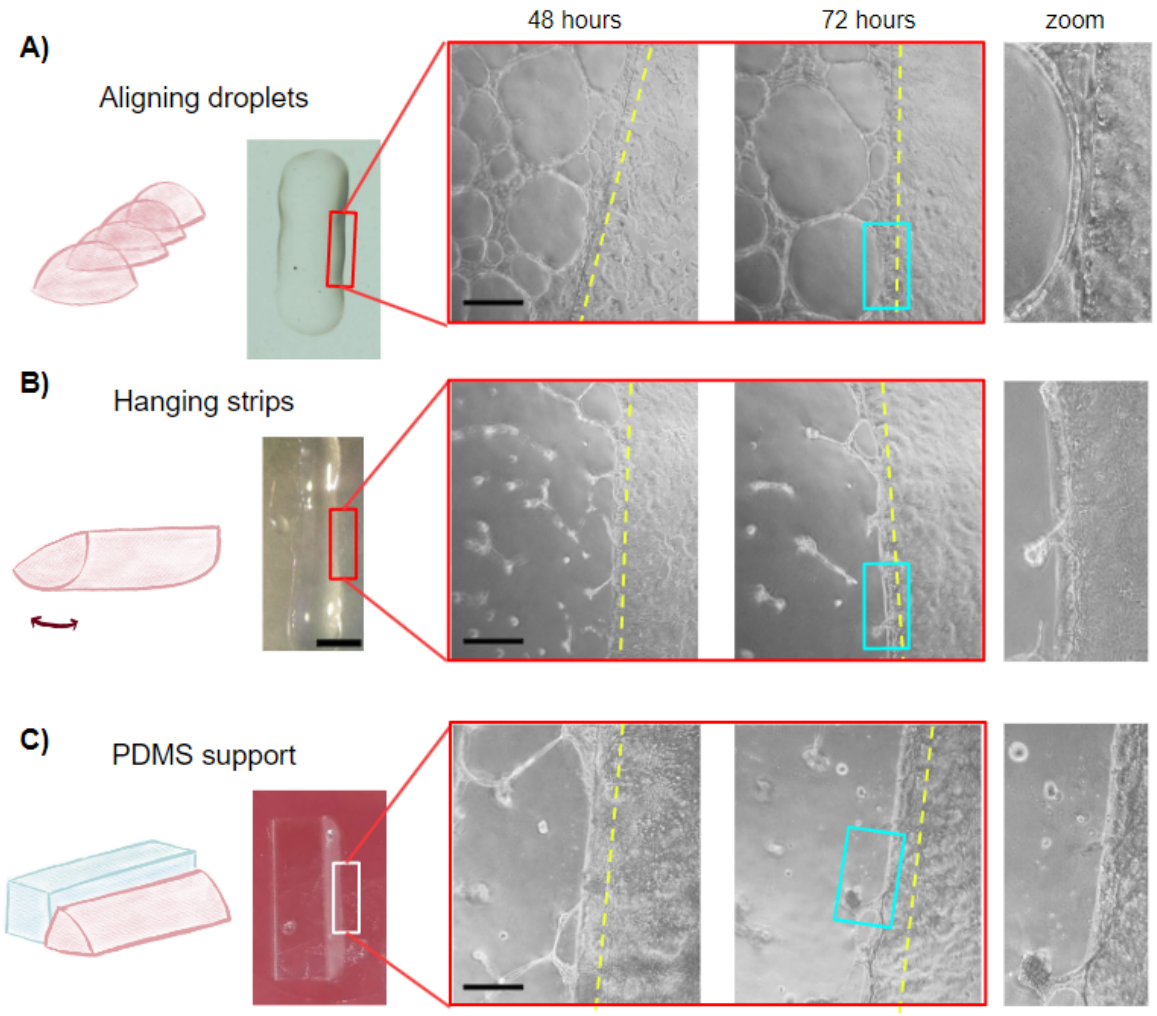

Figure 9. Straight-vessel guidance fabrication strategies. GelTrex deposits were engineered in three different ways for TSEC culture: A) aligned semi-coalescing domes, B) hanging strip, and C) alongside a PDMS scaffold support. After 48 hours, cords are visible at the edge of the architectures (yellow dashed lines). Typical vasculogenesis networks (A) or aggregates (B-C) are visible in the central regions. Scale bar = 500 µm. The right column shows zooms of the edge after 72 hours of culture. The characteristic ECM displacement of the folding step is similar to those of Figure 2 and 5.